

Radiative cooling of laser ablated vapor plumes: experimental and theoretical analyses

Sy-Bor Wen^{a)}, Xianglei Mao^{a)}, Ralph Greif^{b)}, Richard E. Russo^{a)}

Abstract

A study was made of the cooling of the laser induced vapor plume in background air. The temperature and size variations of the vapor plume were determined from spectroscopic measurements during the first few tens of micro-seconds after the laser pulse. Experiments were carried out over a range of laser spot sizes and energies. The energy transport by thermal radiation from the vapor plume to the background air and to the test sample was formulated. Spectral line by line calculations were made (a) calculating the detailed line emission profiles (valid for all optical depths), as well as by (b) dividing the lines into being either optically thin or optically thick. The calculations agreed with one another and with the experimental results for the decreasing vapor plume temperature. It was also shown that for optically thin conditions, which are often valid for small vapor plumes, that the variation of the surface reflectivity of the test sample had very little effect on the cooling process. For optically thin conditions, the temperature

a) Lawrence Berkeley National Laboratory, Berkeley, CA 94720

b) Department of Mechanical Engineering, University of California, Berkeley, California 94720

Keywords Laser ablation, plasma cooling, thermal radiation

decrease of the vapor plume was independent of the plume size, shape, and position. For

larger optical thicknesses of the vapor plume, the calculations showed that the reflectivity of the sample surface and the size of the vapor plume would dramatically affect cooling of the vapor plume.

Introduction

The dynamics of laser induced vapor plumes have been studied experimentally and theoretically for many years [1-11]. Most of the analyses cover the time interval when the laser beam first irradiates the sample surface to a few microseconds after the laser pulse. Few analyses include heat loss from the vapor plume to the surroundings and none of the analyses study vapor plume cooling over the time interval of a few microseconds to hundreds of microseconds after the laser pulse, which is the time interval studied in this paper. The laser induced vapor plume stops expanding a few microseconds after the laser pulse. During this time period, the predicted size and shape of the vapor plume using previous analyses do not agree with the experimental results [12,13]. We attribute this discrepancy to be due to neglecting heat transport from the high temperature vapor plume to the background gas and to the sample surface. Understanding the cooling processes is important for a number of applications. For example, laser induced breakdown spectroscopy (LIBS) utilizes the spectral line emission during this time interval to obtain the composition of a sample. Improved accuracy can be achieved if the variation of the size and the temperature of the vapor plume, which are strong functions of time and have strong effects on the spectral line emission, are known during this time interval. The variation of both the size and temperature of the vapor plume are determined in the present work. For material deposition and nanostructure generation with pulsed lasers, it is important to understand and to control the vapor plume cooling process. The material properties of deposition and nanostructure generation are strongly affected by the cooling rate of the vapor plume.

During vapor plume cooling, which occurs after the initial expansion stage of the vapor plume, the external shockwave will be very weak and beyond the vapor plume front. The pressure of the vapor plume approaches that of the background gas and is unaffected by the backpressure of the external shockwave. The vapor plume should approach local thermal equilibrium during this interval. For the vapor plume, the ideal gas relation,

$$p = nk_B T$$

can be used with the pressure equal to that of the background gas.

The heat affected zone within the vapor plume due to conduction of the vapor plume to the surrounding gas and to the sample is of the order $\sqrt{\alpha\tau}$ where α is the thermal diffusivity of the vapor plume and τ is the time after the laser pulse. α is approximately $1 \times 10^{-3} \text{ m}^2/\text{s}$ for a plasma at a temperature $\sim 10,000\text{K}$ [12,13]. When $\tau \approx 1 \times 10^{-5} - 1 \times 10^{-4} \text{ s}$, the size of the heat affected zone is $\sim 0.1 - 0.3 \text{ mm}$ which is much less than the size of the vapor plume ($1-3 \text{ mm}$).

The diffusion length between the vapor plume and the background air is of the order $\sqrt{D\tau}$, where D is the diffusion coefficient. The diffusion coefficient can be estimated from the mass transport between two different neutral particles [13,14] and yields $\sim 1 \times 10^{-3} \text{ m}^2/\text{s}$ [13,14] at the average temperature between the vapor plume and the background air of $\sim 5,000\text{K}$. The corresponding diffusion length between the high temperature vapor plume and the background air is then $\sim 0.1 - 0.3 \text{ mm}$ when $\tau \approx 1 \times 10^{-5} - 1 \times 10^{-4} \text{ s}$. The diffusion length within the vapor plume may be slightly over estimated because the vapor plume shrinks inward with a speed $\sim 100 \text{ m/s}$ during this time interval. As a result, the diffusion length should be even smaller in comparison to the size of the vapor plume in this interval because the inward mass diffusion from the background gas to the vapor plume is in the same direction as the shrinking vapor plume; both point inward to the center of the vapor plume.

Since the conduction and diffusion lengths are both small compared to the size of the vapor plume during this interval, the high temperature vapor plume can be considered as an isothermal high temperature hemisphere. It is shown in the simulation that thermal radiation is the dominant mechanism which contributes to the temperature decrease during this time interval. Thermal radiation is one of the important mechanisms which determine the change in size of the vapor plume during the cooling process.

Analysis

The analysis studies the cooling rate of the laser induced vapor plume with background air from a few microseconds to about one hundred microseconds after the laser pulse. During this interval, the pressure of the vapor plume is close to the background air pressure; the speed of the external shockwave is close to the sound speed [4] and the temperature decreases from $\geq 10,000\text{K}$ to the order of the boiling temperature of the sample. Since the temperature is high and the conduction and diffusion lengths are small compared to the size of the vapor plume during this interval, a uniform temperature vapor plume is used to determine the thermal radiation. By assuming that the interaction between the sample surface and the vapor plume is small, a hemispherical vapor plume can be used in the simulation [3,4].

The plume approaches local thermal equilibrium in the noted time interval because the collision time between electrons and atoms is much smaller than $1 \mu\text{s}$. Hence, Saha's equations are used to determine the ratios between the number densities of the electrons and ions.

The ideal gas relation, energy equation, mass conservation of the vaporized material, Saha's equations, and electric neutrality are used to determine seven variables: n_e , the

electron density; n_I , the neutral density; n_i , the density of ions at charge stage i , which has $(i-1)$ additional charges; T , the temperature of the vapor plume; and R , the spherical radius of the vapor plume. All quantities listed above are functions of time after the laser pulse. The equations used are:

$$p = (n_I + n_{II} + n_{III} + n_{IV} + n_e)kT \quad (1.1)$$

$$\rho c_p \frac{\partial T}{\partial t} = Q_{rad}/V, \quad (1.2)$$

$$(n_I + n_{II} + n_{III} + n_{IV}) \frac{2\pi R^3}{3} = N_{atom} \quad (1.3)$$

$$\frac{n_e n_{II}}{n_I} = \frac{2g_{II}}{g_I} \left(\frac{2\pi m_e kT}{h^2} \right)^{3/2} e^{-(E_{II} - \Delta E_{II})/kT} \quad (1.4)$$

$$\frac{n_e n_{III}}{n_{II}} = \frac{2g_{III}}{g_{II}} \left(\frac{2\pi m_e kT}{h^2} \right)^{3/2} e^{-(E_{III} - \Delta E_{III})/kT} \quad (1.5)$$

$$\frac{n_e n_{IV}}{n_{III}} = \frac{2g_{IV}}{g_{III}} \left(\frac{2\pi m_e kT}{h^2} \right)^{3/2} e^{-(E_{IV} - \Delta E_{IV})/kT} \quad (1.6)$$

$$n_e = n_{II} + 2n_{III} + 3n_{IV} \quad (1.7)$$

where k is the Boltzmann constant, P is the gas pressure which is equal to the background gas pressure. T is the vapor plume temperature. ρ is the total gas mass density, c_p is the heat capacity, and Q_{rad}/V is the radiative heat transfer per unit volume.

A uniform temperature profile is assumed for the hemispherical vapor plume, and heat conduction and diffusion are omitted. As a result, the energy equation (1.2) can be written as

$$\frac{d \left[\frac{5}{2} kT (n_I + n_{II} + n_{III} + n_{IV} + n_e) \times \frac{2\pi}{3} R^3 \right]}{dt} = Q_{rad} \quad (1.8)$$

where Q_{rad} is the radiative heat loss of the vapor plume from all surfaces. If the surface of the sample is purely reflective, then

$$\begin{aligned}
& \frac{d \left[\frac{5}{2} kT (n_I + n_{II} + n_{III} + n_{IV} + n_e) \times \frac{2\pi}{3} R^3 \right]}{dt} = 2\pi R^2 \times q_{rad} \\
& \frac{d \left(\frac{5\pi}{3} R^3 P_{atm} \right)}{dt} = 2\pi R^2 \times q_{rad} \\
& \frac{dR}{dt} = \frac{2q_{rad}}{5P_{atm}}
\end{aligned} \tag{1.9}$$

where q_{rad} is the radiative heat transfer per unit area from the hemispherical side of the vapor plume. The radiative heat transfer is composed of line emission, free-free emission, and free-bound emission. All three mechanisms are considered in this analysis but according to previous studies [15], line emission is the dominant mechanism at this temperature and pressure. The equilibrium composition of a pure copper plasma over the temperature range from 5000 to 25000K is presented in Fig. 1. Under this temperature with one atmosphere gas pressure, ions with higher than second order ionization make up only a very small part of the total number density of pure copper vapor. Hence, in the calculation of the radiation heat transfer, only the spectral lines from Cu_I and Cu_{II} were considered.

The relations used in evaluating the emissivity from the line and continuum emission mechanisms are presented in the following sections.

I. Radiation transport mechanisms

1. Line emission (bound-bound transitions)

The spectral emission coefficient of an individual line is [15,16],

$$\varepsilon_{L,\nu} = \frac{h\nu_{ul}}{4\pi} A_{ul} n_u P_\nu \tag{1.10}$$

where A_{ul} is the transition probability from the upper energy level u to the lower energy level l , n_u is the upper state population density which can be determined by the Boltzmann relation as

$$n_u = \frac{ng_u}{U} e^{-(E_u - \Delta E_u)/kT} \tag{1.11}$$

ν_{ul} , centerline frequency, is given as

$$\nu_{ul} = \frac{E_u - E_l}{h} \tag{1.12}$$

P_v is the line profile of each spectral line. Since the temperature ranges from 5K to 10K over the time scale of interest, neither a Lorentz or Gaussian profile can fit the spectral line well in the whole temperature range since both Doppler and Stark broadening should be considered over this large temperature interval. Hence, a Voigt profile was used. Calculating the integral for the precise Voigt profile is computationally expensive, so an approximate formula provided by Whitting was used here [17]. The normalized line profile P_v is

$$P_v = \frac{1}{w_v \left[1.065 + 0.447 \left(\frac{w_L}{w_v} \right) + 0.058 \left(\frac{w_L}{w_v} \right)^2 \right]} \cdot \left\{ \left(1 - \frac{w_L}{w_v} \right) \exp \left[-2.772 \left(\frac{v_{ul}^2 / \nu - \nu}{w_v} \right)^2 \right] + \left(\frac{w_L}{w_v} \right) \frac{1}{1 + 4 \left(\frac{v_{ul}^2 / \nu - \nu}{w_v} \right)^2} \right. \\ \left. + 0.016 \left(1 - \frac{w_L}{w_v} \right) \left(\frac{w_L}{w_v} \right) \left[\exp \left[-0.4 \left(\frac{v_{ul}^2 / \nu - \nu}{w_v} \right)^{2.25} \right] - \frac{10}{10 + \left(\frac{v_{ul}^2 / \nu - \nu}{w_v} \right)^{2.25}} \right] \right\} \quad (1.13)$$

where the Voigt half-width can be expressed in terms of the Lorentz half-width, w_L , and Gaussian half-width, w_g , as

$$w_v = \frac{w_L}{2} + \sqrt{\frac{w_L^2}{4} + w_g^2} \quad (1.14)$$

Four types of line broadening were considered [9,10,11,12].

(a) Doppler broadening (Gaussian shape)

The full width at half maximum due to Doppler broadening can be expressed as,

$$w_g = 2(\ln 2)^{1/2} \frac{v_{ul}}{c} \left(\frac{2kT}{M} \right)^{1/2} \quad (1.15)$$

where M is the atomic weight (40 for copper).

(b) Resonance broadening (Lorentz shape)

The full width at half maximum due to resonance broadening can be expressed as,

$$w_{res} = 2.418 \times 10^2 \frac{f_{lu} N_l}{\nu_{lu}} \left(\frac{g_l}{g_u} \right)^{1/2} \quad (1.16)$$

where f_{lu} is the oscillator strength of the resonant levels; g_l and g_u are the statistical weight of ground state and resonance levels respectively.

(c) van der Waals broadening (Lorenz shape)

The full width at half maximum due to van der Waals broadening can be expressed as,

$$w_{vw} = \frac{8.16 C_6^{2/5} \bar{V}^{3/5} n_l}{2\pi} \quad (1.17)$$

where C_6 is the van der Waals constant calculated using the hydrogenoid approximation [18]; \bar{V} is the mean speed of electron.

(d) Stark broadening

An accurate value for Stark broadening using the semiclassical or semiempirical method is complex and is not the main focus of this paper. Instead, a simpler formula was used and is based on the assumption that each perturbation energy level is far away from the line being analyzed [22]. Under this assumption, the full width at half maximum due to stark broadening can be expressed as,

$$w_s = 0.443 \times 10^{-8} \frac{\lambda^2 (cm) n_e (cm^{-3})}{2\pi T^{1/2}} (\bar{R}_{uu}^2 + \bar{R}_{ll}^2) \quad (1.18)$$

where

$$\bar{R}_{ii}^2 \approx \frac{1}{2} \left(\frac{n_i^*}{Z} \right)^2 [5n_i^{*2} + 1 - 3l_i(l_i + 1)]$$

with n_i^* is the effective principal quantum number as

$$n_i^{*2} = Z^2 \frac{E_H}{(I - E_i)}$$

E_i is the empirical excitation energy, and I is the ionization energy

2. Free-free continuum emission (Bremsstrahlung)

2-1. Electron-ion free-free continuum emission

The spectral emission coefficient for electron-ion free-free transitions is given by

$$\varepsilon_{f-f,\nu}^{ei} = 5.44692 \times 10^{-52} \sum_z \frac{(Z-1)^2 n_z n_e}{T^{1/2}} e^{-h\nu/kT} \bar{G}_Z \quad (1.19)$$

with \bar{G}_Z the free-free Gaunt factor which is as [6,10]

$$\bar{G}_Z = 1 + 0.1728 \left[\frac{h\nu}{E_H (Z-1)^2} \right]^{1/3} \left[1 + \frac{2k_B T}{h\nu} \right]$$

2-2. Electron-atom free-free continuum emission

The spectral emission coefficient for electron-atom free-free transitions is given by [20,23]

$$\varepsilon_{f-f,\nu}^{ea} = 3.4213 \times 10^{-43} n_1 n_e T^{3/2} \bar{G} \quad (1.20)$$

with

$$\bar{G} = \bar{\sigma}(T) \left[1 + \left(1 + \frac{h\nu}{kT} \right)^2 \right] e^{-h\nu/kT}$$

where $\bar{\sigma}(T)$ is the electron-neutral collision cross section [24].

3. Free-bound emission (radiative recombination)

When an ion captures an additional electron, light energy should be released due to energy and momentum conservation as

$$Cn^{j+} + e^- \rightarrow Cn^{(j-1)+} + h\nu \quad (1.21)$$

where j is the charge number of the unreacted ion. The emissivity at frequency ν can be expressed as [22,23]

$$\varepsilon_{f-b,\nu} = 5.44692 \times 10^{-52} \sum_z \frac{(Z-1)^2 n_z n_e}{T^{1/2}} \bar{G}_{Zb} \quad (1.22)$$

with

$$\begin{aligned} \bar{G}_{Zb}(\nu, T) = & 1 - 0.1728 \left[\frac{h\nu}{E_H (Z-1)^2} \right]^{1/3} \left[1 - \frac{2kT}{h\nu} \right] \\ & - e^{h\nu/kT} \left\{ 1 + 0.1728 \left[\frac{h\nu}{E_H (Z-1)^2} \right]^{1/3} \left[1 - \frac{2kT}{h\nu} \right] \right\} \end{aligned}$$

By using Kirchhoff radiation law, the emission coefficient, ε_v , is related to the absorption coefficient, K_v , according to

$$\frac{\varepsilon_v}{K_v} = B_v(T) = \frac{2h\nu^3}{c^2} \frac{1}{e^{-h\nu/kT} - 1} \quad (1.23)$$

II. General radiation transport (for all optical depths)

The hemispherical spectral emissive flux, e_v , is given by [21]

$$e_v = 2\pi \int_0^{\pi/2} i(\theta) \cos \theta \sin \theta d\theta$$

When the sample surface is perfectly reflective, $\rho = 1$, at all wavelengths, e_v can be expressed as

$$\begin{aligned} e_v &= 2\pi \int_0^{\pi/2} B_v [1 - \exp(-K_v 2R \cos \theta)] \cos \theta \sin \theta d\theta \\ &= 2\pi \int_0^1 B_v [1 - \exp(-K_v 2R \cos \theta)] \cos \theta d \cos \theta \\ &= 2\pi B_v \left[\frac{-1 + \frac{(K_v 2R)^2}{2} + e^{-K_v 2R} (1 + K_v 2R)}{(K_v 2R)^2} \right] \end{aligned} \quad (1.24)$$

The radiative heat transfer is given by

$$Q_{rad} = 2\pi R^2 \int_0^\infty e_v d\nu \quad (1.25)$$

To determine the radiative heat transfer when the sample surface is not purely reflective, surface absorption must be considered. Radiative heat transfer can then be expressed as

$$\begin{aligned} Q_{rad} &= Q_{rad1} + Q_{rad2} = 2\pi R^2 \int_0^\infty (1 - \rho_v) B_v G_1(K_v R) d\nu \\ &\quad + 2\pi R^2 \int_0^\infty \left\{ \rho_v B_v [G_3(K_v R) - G_2(K_v R)] + B_v G_2(K_v R) + B_v G_4(K_v R) \right\} d\nu \end{aligned} \quad (1.26)$$

Here Q_{rad1} and Q_{rad2} represent radiative heat transfer from the lower circle and the upper hemisphere of the vapor plume, respectively. G_1 , G_2 , G_3 , and G_4 are geometric factors which are functions of optical thickness ($2K_v R$) and are defined in appendix A, which includes a detailed derivation and tabulated values. Since e_v , G_1 , G_2 , G_3 , and G_4 are all sensitive functions of frequency, and change rapidly near the frequencies at

the center of each spectral line, the line-by-line method [15] was applied here, which divides the line spectrum into fine divisions and performs the numerical integration of Eqs. (1.25) and (1.26). Following [15], the number of divisions of the spectrum is doubled until the numerical integration converges to a steady value.

Radiation transport is commonly solved in terms of either diffusive approximation for an optically thick medium or in terms of a thin-layer approximation for an optically thin medium. However, the equations listed above are valid for all optical depths. With the line by line method [15] used in this study, radiative transport of the vapor plume can be solved from the above equations without any assumption in the optical depth of the vapor plume. The following section considers limiting conditions for radiation transport.

III. Limiting radiation transport (lines are either optically thin, $K_v R < 1$, or optically thick, $K_v R > 1$)

The line by line method resolves overlapping of the spectral lines. However, very fine spectral divisions are required with this method which makes the calculation of thermal radiation difficult and time consuming; which is especially important when trying to combine radiative transport with complex gas dynamics phenomena. Therefore, an approach which is more computationally efficient is proposed in this section; namely, to divide the spectral lines into optically thin ($K_v R < 1$) or optically thick ($K_v R > 1$) conditions. For optically thin lines, the thermal radiation heat transfer is given by [16]

$$Q_{rad, opti\ thin} = \underbrace{2\pi R^2 \sum_Z \sum_i \frac{h\nu A_{i,Z} g_{i,Z} n_Z}{3 Q_Z} e^{-E_{i,Z}/k_B T}}_{\text{optically thin lines}} \quad (1.27)$$

where Z is the order of ionization; i is the number of spectral line; Q is the partition function; and g is the statistic weight. For optically thick lines, the thermal radiation heat transfer can be approximated by [30]

$$Q_{rad, opti\ thick} = 2\pi R^2 \underbrace{\sum_Z \sum_i \pi B_v w_{vog}}_{\text{optically thick lines}} \quad (1.28)$$

for a purely reflective sample surface, which is a good approximation for copper at the wavelengths of thermal radiation. The continuum thermal radiation heat transfer, which is always optically thin for our conditions, can be expressed as

$$Q_{rad, con} = \underbrace{\frac{8\pi^2}{3} R^3 \int_0^\infty \varepsilon_{v, con} d\nu}_{\text{continuum emission}} \quad (1.29)$$

where $\varepsilon_{v, con}$ is the spectral emission coefficient due to continuous emission. Thus, the

total radiative heat transfer can be obtained from

$$Q_{rad} \approx \underbrace{2\pi R^2 \sum_Z \sum_i \frac{h\nu A_{i,Z} g_{i,Z} n_Z}{3 Q_Z} e^{-E_{i,Z}/k_B T}}_{\text{optically thin lines}} + \underbrace{2\pi R^2 \sum_Z \sum_i \pi B_\nu w_\nu}_{\text{optically thick lines}} + \underbrace{\frac{8\pi^2}{3} R^3 \int_0^\infty \varepsilon_{\nu,con} d\nu}_{\text{continuum emission}} \quad (1.30)$$

Since the integrand in Eq. (1.29) or Eq. (1.30) does not change as strongly as the integrand in Eqs. (1.25) and (1.26), a coarse spectral division can be used when performing the integration of Eq. (1.29). Compared to Eqs. (1.24) and (1.25), using Eq.(1.29) saves considerable computational time.

For completeness, it is pointed out that most of the spectral lines are optically thin. In the present study, only approximately 300 of the 5665 lines were optically thick ($K_\nu R > 1$) during the cooling process.

The physical properties for the present analysis are obtained from the CRC handbook [28] and from the tables of Kurucz and Peytremann [29].

Experimental system

The experimental system is shown in Figure 2. A Nd:YAG laser (New Wave Research, Minilase II) operating at 1064 nm with a 4-ns pulse-duration was used as the ablation source. The laser beam was focused using a quartz lens on the copper sample to a spot diameter of $\sim 170 \mu\text{m}$. The experiments were performed in atmospheric pressure air. The laser energy was varied from 10 to 120 mJ. A lens was used to image the laser-induced plasma onto the entrance slit of a Czerny-Turner spectrometer (Jobin Yvon, HR460). Spectral emission was detected with an Intensified Charge-Coupled Device (ICCD) system with 1024×1024 pixels (Princeton Instruments, PI MAX 1024 Gen II). This detection system provided a spectral window of $\sim 40 \text{ nm}$ and a resolution of $\sim 0.1 \text{ nm}$, using an entrance slit width of 200 microns (Fig. 3) and grating with 600 grooves/mm. The dark current background of the ICCD detector was subtracted from the measured spectroscopic data for each measurement. The emission intensity was spatially integrated. A delay generator (SRS, DG 535) was used to synchronize the delay time between the laser and the ICCD. Gating the ICCD and changing the time enabled the images and spectra to be temporally resolved. The gate width was set at ten percent of the delay time. A photodiode and a digitizing oscilloscope were used to calibrate the time delay. Plume temperature and line intensity were correlated from the following relation under the optically thin limit [25],

$$\frac{\varepsilon_1}{\varepsilon_2} = \frac{\lambda_2}{\lambda_1} \frac{A_{ul,1}}{A_{ul,2}} \exp\left(-\frac{E_{u,1} - E_{u,2}}{kT}\right) \quad (2.1)$$

From Eq. (2.1), the temperature of the vapor plume can be determined from the intensities of two spectral lines.

The spectral emission lines of Cu(I) at 511.19, 515.32, and 529.81 nm were used for determining the plasma temperature because the intensities of these lines remain sufficiently large to permit accurate detection by ICCD after the laser pulse. Self absorption at 515.32 nm is strong before $\sim 10 \mu s$, and its line shape cannot be fit by the Lorentz profile before this time. After $\sim 10 \mu s$ the intensity of 529.81 nm line is weak. Therefore, for times less than $10 \mu s$ after the laser pulse, the temperatures were determined by using the 511.19 and 529.81 nm lines. For $t \geq 10 \mu s$ after the laser pulse, the temperatures were evaluated from the 511.19 and 515.32 nm lines.

In addition to the temporal variation, the emission intensity ratio between two spectral lines changes from the top to the bottom of the vapor plume (Fig. 4). Therefore, the spatial temperature variation from the top to the bottom within the vapor plume should be evaluated first through the emission intensity ratio of spectral lines at each position. Then, the characteristic temperature of a vapor plume at a certain image time is taken as the spatially average temperature throughout the effective region of the vapor plume (Figs. 4 and 5). The effective region for the temperature evaluation is defined as the spatial region where the emission intensity remains at a value larger than 10 percent of the maximum emission of the 515.32nm line. This region represents the majority of vaporized material. By doing so, the dark region, which appears when the vapor plume detaches from the sample, does not contribute to the temperature measurement. The temperature of the vapor plume within the emission region is almost uniform (Fig. 5). This measurement is consistent with the assumption that the vapor plume has a uniform temperature as used in the simulation.

Results and discussion

Using equations (1.1)-(1.30), the temperature of the vapor plume can be determined during the cooling process when the initial temperature and size of the vapor plume are given. For times less than $1 \mu s$ after the laser pulse, the temperature measurements are not repeatable because of the large broadening and overlapping of each spectral line with a pressure of one atmosphere. Therefore, the measured temperature and size of the vapor plume at $2 \mu s$ after the laser pulse are selected as the initial conditions for the simulation. The results of the simulation for the variation of the vapor plume temperature for three different initial temperatures corresponding to laser energies of 10, 20, and 60mJ are presented in Fig. 6. For this range from about 11,000 to 16,000K, the results are relatively insensitive to the value of the initial temperature, T_i . The temperature of the

vapor plume always drops to less than 10,000K within the first $\sim 10\mu s$ no matter how high the initial temperature is at $2\mu s$. From Fig. 1, for temperatures less than 16,000K, the particles are primarily singly ionized and thus are the main contributors to the radiative transport. The measured temperatures for laser energies from 10 to 60mJ are presented in Fig. 7 and are compared with the simulation results. The measured plume temperatures and sizes at $2\mu s$ are used as the initial conditions of the specified laser energies. Overall, the simulation results agree with the measured temperatures using either the 511.19 and 515.32 nm lines or the 511.19 and 529.81 nm lines for the different energies. The experimental data in Fig. 7 show that the highest temperature at $2\mu s$ is $\sim 16,000K$. As the laser energy was increased to approach the 16,000K condition, the further increase in laser energy has little effect on the vapor plume temperature at $2\mu s$. The calculation methods used in this paper also have been used to calculate the composition of Ar plasma and the emission coefficient of Ar under the optically thin limit condition with one atmospherical pressure for different plasma temperatures. The results are in good agreement with the results presented in Ref. [15].

From the experimental and simulation results, four important results are noted.

1. *The effect of optical opacity (optical depth) on radiative cooling*

The optical opacity of the plasma is defined by the value of $K_v R$. For an optically thin plasma, the emission flux from the vapor plume surface, e_v , is proportional to the radius of the vapor plume according to

$$e_v \propto K_v B_v R \quad (3.1)$$

The surface of the vapor plume $\sim R^2$ and the total energy stored in the vapor plume $\sim R^3$. Thus, the rate of change of the vapor plume temperature is given by

$$\begin{aligned} \frac{dT}{dt} &\propto \frac{(\text{surface area of vapor plume}) \times (\text{emission flux})}{(\text{volume of vapor plume})} \sim \\ &\frac{O(R^2) \times O(R)}{O(R^3)} \sim O(1) \end{aligned} \quad (3.2)$$

The surface area of the vapor plume is the sum of the hemispherical surface, $2\pi R^2$ and the bottom lower circle, πR^2 of the hemisphere; the volume of the vapor plume is $2\pi R^3 / 3$. Therefore, for the optically thin condition from Eq. (3.2), the rate of temperature decrease of the vapor plume is independent of the size of the vapor plume.

For the optically thick condition, the emission flux of the vapor plume approaches black body radiation, B_v , which is independent of the size of the vapor plume. Thus, for the optically thick condition, the rate of change of the plume temperature is

$$\begin{aligned} \frac{dT}{dt} &\propto \frac{(\text{surface area of vapor plume}) \times (\text{black body flux})}{(\text{volume of vapor plume})} \sim \\ \frac{O(R^2) \times O(1)}{O(R^3)} &\sim O(R^{-1}) \end{aligned} \quad (3.3)$$

Therefore, larger (optically thick) vapor plumes have slower cooling rates.

Shown in Fig. 8a,b is the fraction of the radiative heat transfer from the optically thick lines, $K_v R > 1$, for two laser energies. Approximately 100-300 lines are optically thick during the cooling process. These optically thick lines provide ~30% of the radiative heat loss during the cooling process. Thus, since most of the radiative heat loss (~70%) corresponds to optically thin lines, the size of the vapor plume will not greatly change the rate of cooling of the vapor plume, cf. Eq. (3.2). Hence, the dominant variable for radiative cooling is the initial temperature of the vapor plume for a given sample material which helps explain the similarity of the results for all laser energies (cf. fig. 6). To study the sensitivity of the vapor plume cooling rate with respect to the size of the vapor plume, experiments were carried out with different spot sizes and laser energies to obtain about the same vapor plume temperature at $2\mu s$ after the laser pulse. It is emphasized that this is an experimental challenge because there is no simple relation for determining the plume temperature as a function of spot size and laser energy. Two sets of data are shown in Figs. 9 (a,b). The experiments show a similar rate of temperature decrease for the two vapor plumes having approximately the same initial temperatures but different sizes, confirming the dominance of optically thin radiation (which is independent of the size of the vapor plume).

2. Sample surface reflectivity

The sample surface reflectivity can influence the radiative heat transfer by affecting (1) the fraction of incident thermal radiation that is absorbed by the sample and (2) the fraction of thermal radiation that passes through the hemispherical surface of the vapor plume in the direction shown in Fig. 10. Gas emission is included in this transport and the surface is considered to be specular in the present study. By tracing an optical path that originates from the hemispherical surface of the vapor plume (e.g. point A in Fig. 10), striking the sample surface and then passes through the vapor plume, the spectral energy loss per unit area per unit solid angle from the hemispherical vapor plume along this optical path is

$$\begin{aligned}
\Delta q_v &= \Delta q_{v,(absorbed)} + \Delta q_{v,(passing\ through)} \\
&= \left\{ (1 - \rho_v) B_v [1 - \exp(-K_v(L - S))] \right\} + \\
&\quad \left\{ \rho_v B_v [1 - \exp(-K_v(L - S))] \exp(-K_v S) + B_v [1 - \exp(-K_v S)] \right\}
\end{aligned} \tag{3.4}$$

The first term, $\Delta q_{v,(absorbed)}$, is absorption of the incident energy by the sample surface, and the second term, $\Delta q_{v,(passing\ through)}$, is the energy which passes through the hemispherical vapor plume surface. When the reflectivity of the sample surface increases, the absorption of the incident energy, $\Delta q_{v,(absorbed)}$, will decrease, but the energy passing through the hemispherical surface of the vapor plume surface, $\Delta q_{v,(passing\ through)}$, will increase, and the reverse is true for a decrease in the reflectivity of the sample surface. Again, the gas emission also is being included in this transport. For the optically thin limit,

$$\begin{aligned}
[1 - \exp(-K_v(L - S))] &\approx K_v(L - S) \\
[1 - \exp(-K_v S)] &\approx K_v S
\end{aligned} \tag{3.5}$$

Then, the spectral energy loss per unit area per unit solid angle from the hemispherical vapor plume along the optical path starting at point A in Fig. 10 becomes

$$\begin{aligned}
\Delta q_v &= \Delta q_{v,(absorbed)} + \Delta q_{v,(passing\ through)} \\
&= \left\{ (1 - \rho_v) B_v [K_v(L - S)] \right\} + \left\{ \rho_v B_v [K_v(L - S)] + B_v K_v S \right\} \\
&= B_v K_v L
\end{aligned} \tag{3.6}$$

Therefore, the change of $\Delta q_{v,(absorbed)}$ due to the surface reflectivity balances the change of $\Delta q_{v,(passing\ through)}$, and there is no net effect of the reflectivity of the sample surface under the optically thin condition. Since ~70% of the thermal emission is considered to be optically thin, which is independent of the reflectivity of the sample surface, the surface reflectivity of the sample is not a critical quantity and for convenience may be approximated by a value of $\rho = 1$ for all wavelengths in the calculation of radiative energy loss (Eq. (1.25)). The closed form result is then

$$Q_{rad} = 2\pi R^2 \int_0^\infty \frac{B_\nu}{(2K_\nu R)^2} \left[-1 + \frac{(2K_\nu R)^2}{2} + e^{-2K_\nu R} (1 + 2K_\nu R) \right] d\nu \quad (3.7)$$

There is little error in this result for the radiative energy loss (assuming $\rho = 1$) compared to that including the surface reflectivity effect in Eq. (1.26). Figure 11 shows the spectral radiative heat transfer ratio for an ideal absorbing black surface, $\rho = 0$, divided by a perfectly reflecting surface, $\rho = 1$, as a function of optical depth, $K_\nu R$. When $K_\nu R = 1$, there is $\sim 15\%$ change in the spectral thermal radiation between $\rho = 0$ and $\rho = 1$ for the sample surface.

Radiation heat transfer from a hemispherical vapor plume with a purely reflecting sample surface, $\rho = 1$, which is a good approximation for an optically thin vapor plume, is the same as the radiation heat transfer from a spherical vapor plume. Therefore, the plume cooling rate should not be sensitive to the shape and position of the vapor plume relative to the sample surface for the nearly optically thin experimental conditions. It was also concluded that the cooling rate of the vapor plume was not sensitive to the size of the vapor plume (as discussed in section 1). Thus, the cooling rate of the vapor plume is not sensitive to the size, shape, and position of the vapor plume.

3. *Simulation Error*

A source of error in our simulation compared to the actual experimental conditions is the assumption of a hemispherically shaped vapor plume staying on the sample surface. Due to frictional flow between the evaporated material and the stationary sample, a velocity gradient establishes a vortex ring within the vapor plume [26,27]. This vortex ring provides a lift force on the vapor plume and pushes the high temperature vaporized material away from the sample surface. Therefore, the high emission region of the vapor plume moves away from the sample surface during the first few tens of microseconds (depending on the laser energy) after the laser pulse (Figure 12). According to parts one and two which determines that the cooling rate of vapor plume is not sensitive to the size, shape, and position of the vapor plume, this should not cause a significant error in the predicted decrease of the vapor plume temperature, although the lift could have an effect on the predicted size of the vapor plume during the cooling process (Fig. 13).

A second error in our simulation is the assumption that thermal radiation is the only heat transfer mechanism during vapor-plume cooling. This assumption could explain why the simulated temperature decrease is lower than the experimental data when the temperature of the vapor plume is lower than ~ 5000 - 6000 K. The difference in the temperature predicted and the experimental data can be as large as 1000 K in this range

(Fig. 7). Conduction and diffusion are important compared to radiation at later times (lower temperatures) after the laser pulse. When analyzing nanoparticle generation in laser generated plasmas, which occurs at about 3000K for the copper vapor plume under normal background air pressure, conduction and diffusion should no longer be neglected in the simulation.

Another error comes from the unavailability of certain physical quantities for the numerical simulation. Two of these physical quantities are Biberman factors which are used for the calculation of the continuum emission and the Stark broadening width for the calculation of the line emission [16].

4. *Experimental Error*

Due to the large emission rates of both the 511.19 and 515.32nm lines, the detected emission intensities of both lines are less than the value predicted under the optical thin limit assumption due to self absorption. The values of the emission intensities of the three lines used in the temperature measurements vary according to 515.32nm>511.19nm>529.91nm. Therefore, the amount of self absorption of these three lines gives 515.32nm>511.19nm>529.91nm. As a result, the measured intensity ratio between the 511.19 and 515.32nm lines is increased compared to the idealized intensity ratio without self absorption, while the intensity ratio between the 511.19 and 529.81nm lines is decreased compared to the idealized intensity ratio without self absorption. Therefore, the temperature determined from the 511.19 and 515.32nm lines is less than the actual value and the temperature evaluated from the 511.19 and 529.81nm lines is greater than the actual value. The values of the temperatures from the simulations are in better agreement with the temperatures evaluated from all three lines as the time after the laser pulse increases and the self absorption decreases.

In addition to self absorption, errors in the transition probability, A , are important in evaluating the vapor plume temperature. According to the CRC handbook [27], errors in the transition probabilities are categorized as class C, which means a possible error range of 25%. This could be the primary reason why the temperatures obtained from the two line pairs are different even at low vapor plume temperature when self absorption of the 511.19 and 515.32nm lines are not important.

Conclusions

The cooling of the vapor plume generated by laser ablation is dominated by thermal radiation in the temperature range from tens of thousands Kelvin down to approximately 6000K. This period corresponds to a time interval from $1 \sim 2 \mu s$ to tens of micro-seconds after the laser pulse. About 70 percent of the emission energy comes from optically thin spectral lines; hence, the shape and the reflectivity of the sample surface do not have strong effects on radiation transport. Consequently, a hemispherically shaped vapor plume adjacent to a perfectly reflective sample surface is a good approximation for the analysis of the thermal radiation from the high temperature vapor plume induced by a laser pulse. The temperatures predicted by the analyses are in good agreement with experimental data. The general analysis (good for all optical depths) resolves the overlapping of the spectral lines and continuum emission and provides an accurate value of heat loss from the vapor plume by radiative heat transfer. For the experimental conditions, a simpler method which divides the spectral lines into two groups either optically thin or optically thick and uses the closed form solutions in both extreme situations was also proposed and proves to be valid and in good agreement with the general analysis (valid for all optical depths). The predicted size of the vapor plume did not agree with the experimental values, which may be due to the omission of a vortex ring within the vapor plume in the simulation.

To determine the vapor plume dynamics for larger time scales, gas dynamics must be included. A gas dynamic analysis combined with a cooling analysis should enable the determination of the vapor plume dynamics from a few tens of pico-seconds to tens of micro-seconds after the end of the laser pulse.

Acknowledgement

This work was supported by the U.S. Department of Energy, Office of Basic Energy Sciences, Chemical Sciences Division at the Lawrence Berkeley National Laboratory under contract number DE-AC02-05CH11231.

List of Figures

Figure A-1. Picture description of hemispherical radiation

Figure A-2. The value of G_1 as a function of $K_v R$

Figure A-3. Picture description of the sample side radiation

Figure A-4. The value of $G_3 - G_2$ and $G_2 + G_4$ as functions of $K_v R$

Figure 1. Equilibrium composition of a 1 atm pure copper vapor

Figure 2. Experiment setup for ablating a target and time-resolved imaging of plasma properties.

Figure 3. The spectrometer configuration used to image the plume. A 0.2mm slit was used along the longitudinal direction from the sample surface in order to capture the spatial temperature variation of the vapor plume.

Figure 4. Spatial distribution of the emission intensity within the vapor plume for different spectral lines ($E=100\text{mJ}$, image time= $10\text{ }\mu\text{s}$). Zero corresponds to the position of the sample surface.

Figure 5. Spatial distribution of the temperature within the vapor plume calculated from different spectral lines ($E=100\text{mJ}$, image time= $10\text{ }\mu\text{s}$). Zero corresponds to the position of the sample surface.

Figure 6. Simulation result for the temperature variation of the vapor plume for different laser energies.

Figure 7. Comparison of the simulation results with the measurements of the temperature of the vapor plume for different laser energies, $E(\text{mJ})$. (a) 10mJ (b) 20mJ (c) 30mJ (d) 40mJ (e) 50mJ (f) 60mJ.

Figure 8. (a) Fraction of the optically thick lines contributing to the radiative heat transfer when $E=10\text{mJ}$ (b) Fraction of the optically thick lines contributing to the radiative heat transfer when $E=100\text{mJ}$

Figure 9. Temperature variations of vapor plumes with different spot size and laser energy but with similar initial plume temperature.

Figure 10. Schematic diagram of the radiative heat loss from the vapor plume starting at A which reaches the sample surface and specularly reflects through the vapor plume.

Figure 11. The spectral radiative heat transfer ratio between an ideal absorption surface, $\rho = 0$, and an ideal reflection sample surface, $\rho = 1$

Figure 12. Spectral image of the 515.32nm emission line at different times after the laser pulse with $E=50\text{mJ}$, and $E=100\text{mJ}$ with spot size $\sim 170\text{ }\mu\text{m}$.

Figure 13. Comparison between simulated (by general line-by-line analysis) and experimental results of the vapor plume size under different laser energies.

References

- [1] Y. B. Zel'dovich, Yu. P. Raizer, Physics of Shock Waves and High-Temperature Hydrodynamic Phenomena, Ed. by W. D. Hayes and R. F. Probstein, (Academic Press, London, 1966).
- [2] Anisimov, S.I.; Bauerle, D.; Lukyanchuk, B.S., Phys. Rev. B **48**, 12076-12081 (1993).
- [3] Bulgakov, A. V. and Bulgakova, N. M., Journal of Physics D-Applied Physics **28**(8), 1710 (1995).
- [4] Arnold, N., Gruber, J., and Heitz, J., Applied Physics A-Materials Science & Processing **69**, S87-S93 (1999).
- [5] Itina, T.E.; Hermann, J.; Delaporte, P.; Sentis, M., Marine W, Phys.Rev. E, **62** , pp. 4152 - 4161, (2000).
- [6] T. E. Itina, J. Hermann, P. Delaporte and M. Sentis, Phys. Rev. E, **66**, 066406 (2002).
- [7] Mazhukin, V.I.; Nossov, V.V.; Flamant, G.; Smurov, I., Journal of Quantitative Spectroscopy & Radiative Transfer **73**, 451-460 (2002).
- [8] Mazhukin, V.I.; Nossov, V.V.; Nickiforov, M.G.; Smurov, I., Journal of Applied Physics, 93(1), 56-66 (2003).
- [9] Bogaerts, A.; Chen, Z. Y.; Gijbels, R.; Vertes, A., Spectrochim. Acta B 58 (11), 1867-1893 (2003)
- [10] Mazhukin, V I; Nossov, V V; Smurov, I; Flamant, G, Journal of Physics. D, Applied Physics, 37(2), 185-199 (2004).
- [11] Capitelli, M.; Casavola, A.; Colonna, G.; De Giacomo, A., Spectrochim. Acta B 59 (3): 271-289 (2004).
- [12] Gleizes, A., Gonzalez, J. J., and Freton, P., Journal of Physics D-Applied Physics 38(9), R153-R183 (2005).
- [13] Chapman S. and Cowling T. G., The mathematical Theory of Non Uniform Gases (Cambridge university press, Cambridge, 1958).
- [14] Mills A. F., Mass Transfer, (Prentice Hall, Upper Saddle River, NJ, 2001).
- [15] Menart, J., Heberlein, J., and Pfender, E., Journal of Quantitative Spectroscopy & Radiative Transfer **56**(3), 377 (1996).
- [16] Boulos M. I., Fauchais P., and Pfender E, Thermal Plasmas: Fundamentals and Applications, vol. 1, (Plenum press, New York, 1994).
- [17] Whiting, E. E., Journal of Quantitative Spectroscopy & Radiative Transfer **8**(6), 1379-1384 (1968).
- [18] Lochte-Holtgreven W., Plasma Diagnostics, (AIP press, 1995).
- [19] Griem H. R., Plasma Spectroscopy, (McGraw-Hill, 1964).
- [20] Anders A., A formulary for plasma physics, (Akademie-Verlag Berlin, 1990).
- [21] Siegel R. and Howell J., Thermal radiation heat transfer, 4th ed, (Taylor & Francis, New York, 2002).
- [22] Menzel, D. H. and Pekeris, C. L., Monthly Notices of the Royal Astronomical

Society **96**(1), 0077 (1935).

[23] Venugopalan M., Reactions under Plasma conditions, Vol. 1, (Wiley, New York, NY, 1971).

[24] Trajmar, S., Williams, W., and Srivastava, S. K., Journal of Physics B-Atomic Molecular and Optical Physics **10**(16), 3323 (1977).

[25] Boumans P. W. J. M., Inductively Coupled Plasma Emission Spectroscopy, Part 2: Applications and Fundamentals (John Wiley & Sons, New York, 1987)

[26] Puretzky, A. A., Geohegan, D. B., Schittenhelm, H., Fan, X. D., and Guillorn, M. A., Applied Surface Science **197**, 552 (2002).

[27] Ho, J. R., Grigoropoulos, C. P., and Humphrey, J. A. C., Journal of Applied Physics **78**(7), 4696 (1995).

[28] Lide D. R., CRC Handbook of Chemistry and Physics, 85th ed, (CRC Press, 2004)

[29] Kurucz R. L., Peytremann E., *A Table of Semiempirical gf Values*, Parts I, II, and III, Smithsonian, Astrophysical Observatory Special Report 362 (1975).

[30] Lasher L. E. , Wilson K. H. , Greif R., J. Quant. Spectros. Radiat. Transfer 7: 305–322 (1967).

[31] Penner S. S., Olfe D. B., Radiation and Reentry (Academic Press, New York, 1968)

Appendix

A-1. Radiation to the hemispherical surface of the vapor plume (good for all optical depths)

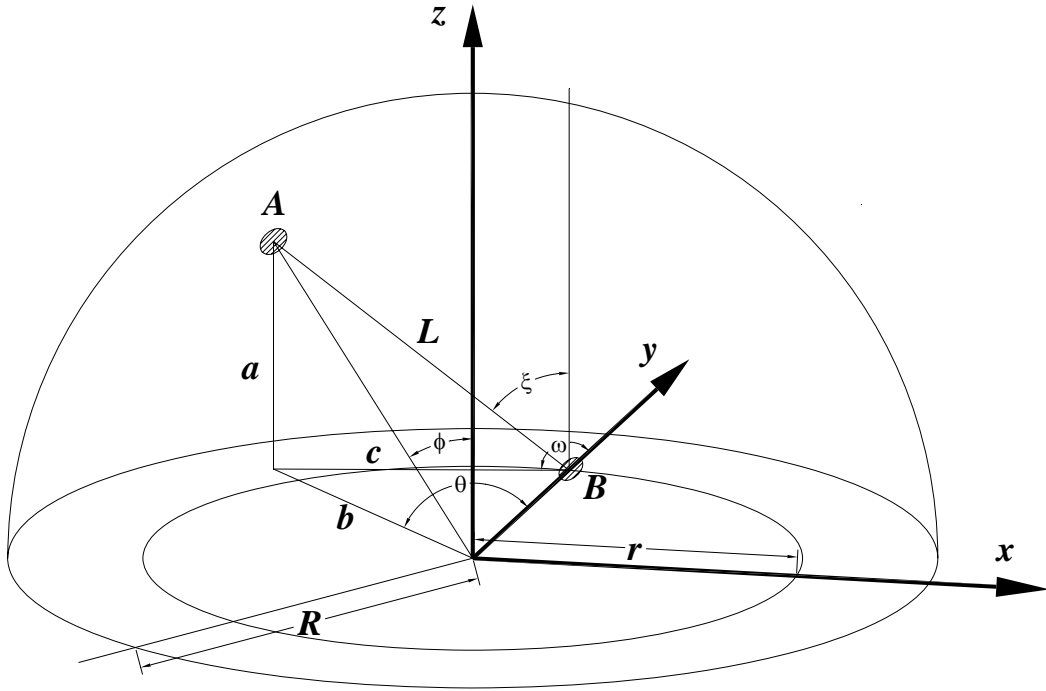


Figure A-1. Picture description of hemispherical radiation

From the triangular relations,

$$a = L \cos \xi$$

$$c = L \sin \xi$$

And

$$b = \sqrt{R^2 - L^2 \cos^2 \xi}$$

Hence,

$$r^2 + L^2 \sin^2 \xi + 2rL \sin \xi \cos \omega = R^2 - L^2 \cos^2 \xi$$

$$\Rightarrow L^2 + 2rL \sin \xi \cos \omega - R^2 + r^2 = 0$$

$$\Rightarrow L = -r \sin \xi \cos \omega + \sqrt{r^2 \sin^2 \xi \cos^2 \omega + R^2 - r^2}$$

From the equation of transfer, the spectral intensity can be expressed as

$$i_\nu = (1 - \rho_\nu) B_\nu (1 - e^{-K_\nu L})$$

After traveling a distance L . Then, the total intensity is

$$i = \int_0^\infty (1 - \rho_\nu) B_\nu [1 - \exp(-K_\nu L)] d\nu$$

And the emissive power is

$$\begin{aligned} e &= \int_0^{2\pi} \int_0^{\pi/2} i \cos \xi \sin \xi d\xi d\omega \\ &= \int_0^{2\pi} \int_0^{\pi/2} \int_0^\infty (1 - \rho_\nu) B_\nu [1 - \exp(-K_\nu L)] d\nu \cos \xi \sin \xi d\xi d\omega \end{aligned}$$

By integrating throughout the bottom surface, the net energy loss from the bottom wall becomes

$$\begin{aligned} Q_1 &= \int_0^R e 2\pi r dr \\ &= \int_0^R \int_0^{2\pi} \int_0^{\pi/2} 2\pi r i \cos \xi \sin \xi d\xi d\omega dr \\ &= \int_0^R \int_0^{2\pi} \int_0^{\pi/2} \int_0^\infty 2\pi r (1 - \rho_\nu) B_\nu [1 - \exp(-K_\nu L)] d\nu \cos \xi \sin \xi d\xi d\omega dr \end{aligned}$$

By defining

$$\begin{aligned} G_1(K_\nu R) &= \int_0^1 \int_0^{2\pi} \int_0^{\pi/2} [1 - \exp(-(K_\nu R)(L/R))] \left(\frac{r}{R}\right) \cos \xi \sin \xi d\xi d\omega d\left(\frac{r}{R}\right) \\ &= \int_0^1 \int_0^{2\pi} \int_0^{\pi/2} \left[1 - \exp\left(-(K_\nu R)\left(-\frac{r}{R} \sin \xi \cos \omega + \sqrt{\frac{r^2}{R^2} \sin^2 \xi \cos^2 \omega + 1 - \frac{r^2}{R^2}}\right)\right)\right] \left(\frac{r}{R}\right) \cos \xi \sin \xi d\xi d\omega d\left(\frac{r}{R}\right) \end{aligned}$$

Then

$$Q_1 = 2\pi R^2 \int_0^\infty (1 - \rho_\nu) B_\nu G_1(K_\nu R) d\nu$$

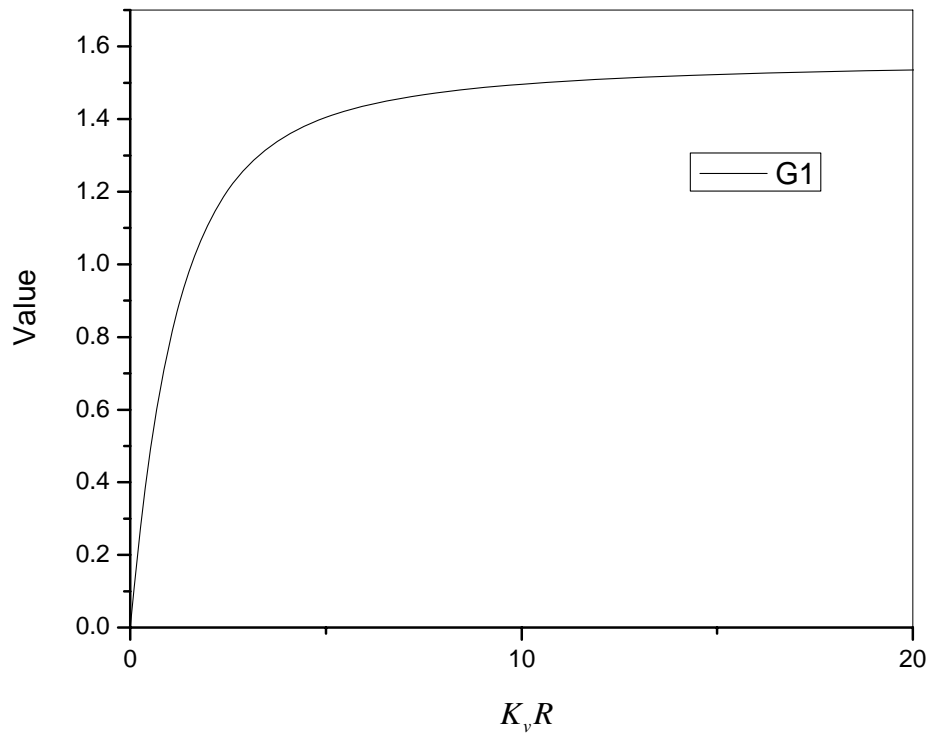


Figure A-2. The value of G_1 as a functions of $K_v R$

A-2. Radiation to the sample surface side of the vapor plume (good for all optical depths)

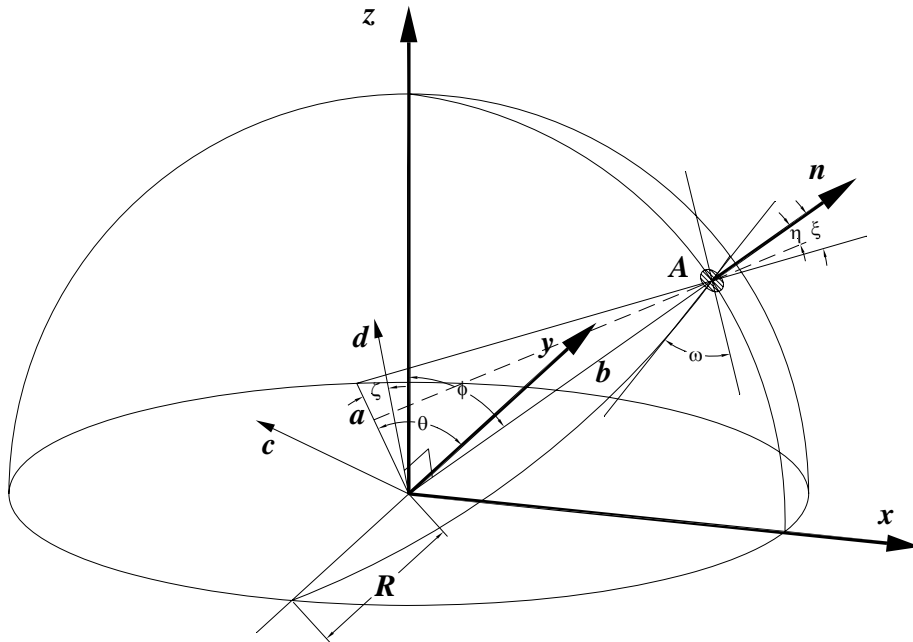


Figure A-3. Picture description of the sample side radiation

When $0 < \omega < \pi$, unit vectors \vec{a} and \vec{b} can be expressed in the Cartesian coordinate as

$$\begin{aligned}\vec{a} &= (-\sin \theta, \cos \theta, 0) \\ \vec{b} &= (\sin \phi, 0, \cos \phi)\end{aligned}$$

The vector \vec{c} which normal to plan of \vec{a} and \vec{b} is

$$\vec{b} \times \vec{a} = (-\cos \phi \cos \theta, -\cos \phi \sin \theta, \sin \phi \cos \theta)$$

And the unit vector \vec{d} normal to \vec{b} and in the plane of \vec{a} and \vec{b} is

$$\frac{\vec{c} \times \vec{b}}{|\vec{c} \times \vec{b}|} = \frac{(-\cos^2 \phi \sin \theta, \cos \theta, -\sin \phi \cos \phi \sin \theta)}{\sqrt{\sin^2 \theta \cos^2 \phi + \cos^2 \theta}}$$

Hence,

$$\cos \omega = \vec{d} \cdot \vec{y} = \frac{\cos \theta}{\sqrt{\sin^2 \theta \cos^2 \phi + \cos^2 \theta}}$$

$$\begin{aligned}\cos \zeta &= \vec{a} \cdot \vec{d} = (\cos^2 \phi \sin^2 \theta + \cos^2 \theta)^{1/2} \\ \zeta &= \cos^{-1} (\cos^2 \phi \sin^2 \theta + \cos^2 \theta)^{1/2}\end{aligned}$$

And

$$\xi = \frac{\pi - \left(\frac{\pi}{2} + \zeta\right)}{2} = \frac{\pi}{4} - \frac{\zeta}{2}$$

For $\eta < \xi$, the directional emission intensity is due to the light source originate from the hemispherical surface and reflects from the sample surface. The light will travel a distance $L - S$ and hit the sample surface; then, it will travel another distance S before moving out of point A.

The relation between S and the radius of the vapor plume R can be expressed in the following relation

$$\frac{R}{\sin\left(\frac{\pi}{2} - \zeta - \eta\right)} = \frac{S}{\sin\left(\frac{\pi}{2} + \zeta\right)}$$

With

$$L = 2R \cos \eta$$

Hence

$$\begin{aligned}
\frac{R}{\cos\left(\cos^{-1}\left(\cos^2\phi\sin^2\theta+\cos^2\theta\right)^{1/2}+\eta\right)} &= \frac{S}{\left(\cos^2\phi\sin^2\theta+\cos^2\theta\right)^{1/2}} \\
\Rightarrow S &= \frac{\left(\cos^2\phi\sin^2\theta+\cos^2\theta\right)^{1/2} R}{\cos\left(\cos^{-1}\left(\cos^2\phi\sin^2\theta+\cos^2\theta\right)^{1/2}+\eta\right)} \\
\Rightarrow L-S &= R \left[2\cos\eta - \frac{\left(\cos^2\phi\sin^2\theta+\cos^2\theta\right)^{1/2}}{\cos\left(\cos^{-1}\left(\cos^2\phi\sin^2\theta+\cos^2\theta\right)^{1/2}+\eta\right)} \right]
\end{aligned}$$

Also, with

$$\frac{\cos\theta}{\cos\omega} = \sqrt{\sin^2\theta\cos^2\phi+\cos^2\theta} = \frac{\cos\phi}{\left(1-\sin^2\phi\cos^2\omega\right)^{1/2}}$$

The above relations can be modified as

$$\begin{aligned}
S &= \frac{\frac{\cos\theta}{\cos\omega} R}{\cos\left(\cos^{-1}\frac{\cos\theta}{\cos\omega}+\eta\right)} \\
L-S &= R \left[2\cos\eta - \frac{\frac{\cos\theta}{\cos\omega}}{\cos\left(\cos^{-1}\frac{\cos\theta}{\cos\omega}+\eta\right)} \right]
\end{aligned}$$

For $\eta > \xi$, the directional emission intensity originate from the hemispherical surface will not hit the sample surface, and the total optical path length is $2R\cos\eta$

When $\pi < \omega < 2\pi$, similar relation of optical path length can be derived as above. Relation between optical path length and azimuthal angles are listed as below

$$\xi = \cos^{-1}\left(\cos^2\phi\sin^2\theta+\cos^2\theta\right)^{1/2}$$

$$\xi' = \frac{\pi - \left(\frac{\pi}{2} - \xi\right)}{2} = \frac{\pi}{4} + \frac{\xi}{2}$$

$$\frac{\cos\theta}{\cos\omega} = \sqrt{\sin^2\theta\cos^2\phi+\cos^2\theta} = \frac{\cos\phi}{\left(1-\sin^2\phi\cos^2\omega\right)^{1/2}}$$

For $\eta < \xi'$

$$S' = \frac{\frac{\cos \theta}{\cos \omega} R}{\cos \left(\cos^{-1} \frac{\cos \theta}{\cos \omega} - \eta \right)}$$

$$L' - S' = R \left[2 \cos \eta - \frac{\frac{\cos \theta}{\cos \omega}}{\cos \left(\cos^{-1} \frac{\cos \theta}{\cos \omega} - \eta \right)} \right]$$

For $\eta > \xi'$, the directional emission intensity originate from the hemispherical surface will not hit the sample surface, and the total optical path length is again $2R \cos \eta$

From the equation of transfer, the spectral intensity can be expressed as

$$i_\nu = \begin{cases} \rho_\nu B_\nu [\exp(-K_\nu S) - \exp(-K_\nu L)] + B_\nu [1 - \exp(-K_\nu S)], & \text{for } \eta < \xi \\ B_\nu [1 - \exp(-K_\nu L)] & , \text{for } \eta > \xi \end{cases}$$

After traveling a distance L . Then, the total intensity is

$$i = \int_0^\infty i_\nu d\nu$$

$$= \begin{cases} \int_0^\infty \left\{ \rho_\nu B_\nu [\exp(-K_\nu S) - \exp(-K_\nu L)] + B_\nu [1 - \exp(-K_\nu S)] \right\} d\nu, & \text{for } \eta < \xi \\ \int_0^\infty B_\nu [1 - \exp(-K_\nu L)] d\nu & , \text{for } \eta > \xi \end{cases}$$

And the emissive power is

$$e = \int_0^{2\pi} \int_0^{\pi/2} i \cos \eta \sin \eta d\eta d\omega$$

$$= \int_0^\infty \int_0^{2\pi} \left\{ \int_0^\xi \left\{ \rho_\nu B_\nu [\exp(-K_\nu S) - \exp(-K_\nu L)] + B_\nu [1 - \exp(-K_\nu S)] \right\} \cos \eta \sin \eta d\eta \right.$$

$$\left. + \int_\xi^{\pi/2} B_\nu [1 - \exp(-K_\nu L)] \cos \eta \sin \eta d\eta \right\} d\omega d\nu$$

By integrating throughout the hemispherical surface, the net energy loss from the hemispherical side becomes

$$\begin{aligned}
Q_2 &= 2\pi R^2 \int_0^{\pi/2} e \sin \phi d\phi \\
&= 2\pi R^2 \int_0^{\pi/2} \int_0^\infty \int_0^{2\pi} \left\{ \int_0^\xi \left\{ \rho_\nu B_\nu [\exp(-K_\nu S) - \exp(-K_\nu L)] + B_\nu [1 - \exp(-K_\nu S)] \right\} \cos \eta \sin \eta d\eta \right. \\
&\quad \left. + \int_\xi^{\pi/2} B_\nu [1 - \exp(-K_\nu L)] \cos \eta \sin \eta d\eta \right\} d\omega d\nu \sin \phi d\phi
\end{aligned}$$

By defining

$$\begin{aligned}
G_2(K_\nu R) &= \int_0^{\pi/2} \int_0^{2\pi} \int_0^\xi [1 - \exp(-(K_\nu R)(S/R))] \cos \eta \sin \eta \sin \phi d\eta d\omega d\phi \\
G_3(K_\nu R) &= \int_0^{\pi/2} \int_0^{2\pi} \int_0^\xi [1 - \exp(-(K_\nu R)(L/R))] \cos \eta \sin \eta \sin \phi d\eta d\omega d\phi \\
G_4(K_\nu R) &= \int_0^{\pi/2} \int_0^{2\pi} \int_\xi^{\pi/2} [1 - \exp(-(K_\nu R)(L/R))] \cos \eta \sin \eta \sin \phi d\eta d\omega d\phi
\end{aligned}$$

Then

$$Q_2 = 2\pi R^2 \int_0^\infty \left\{ \rho_\nu B_\nu [G_3(K_\nu R) - G_2(K_\nu R)] + B_\nu G_2(K_\nu R) + B_\nu G_4(K_\nu R) \right\} d\nu$$

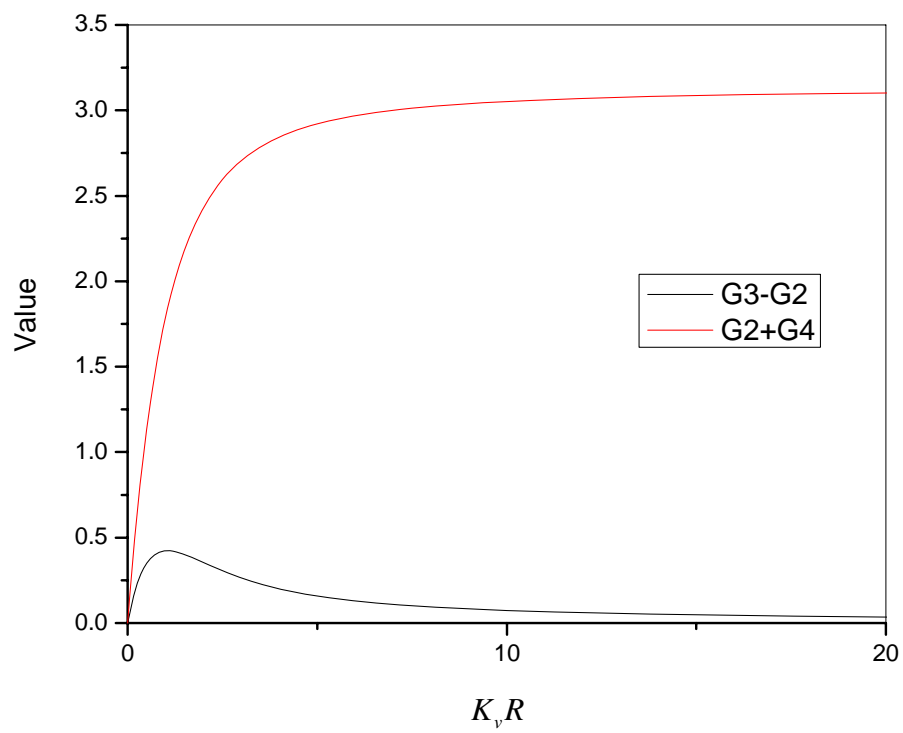


Figure A-4. The value of $G_3 - G_2$ and $G_2 + G_4$ as functions of $K_v R$

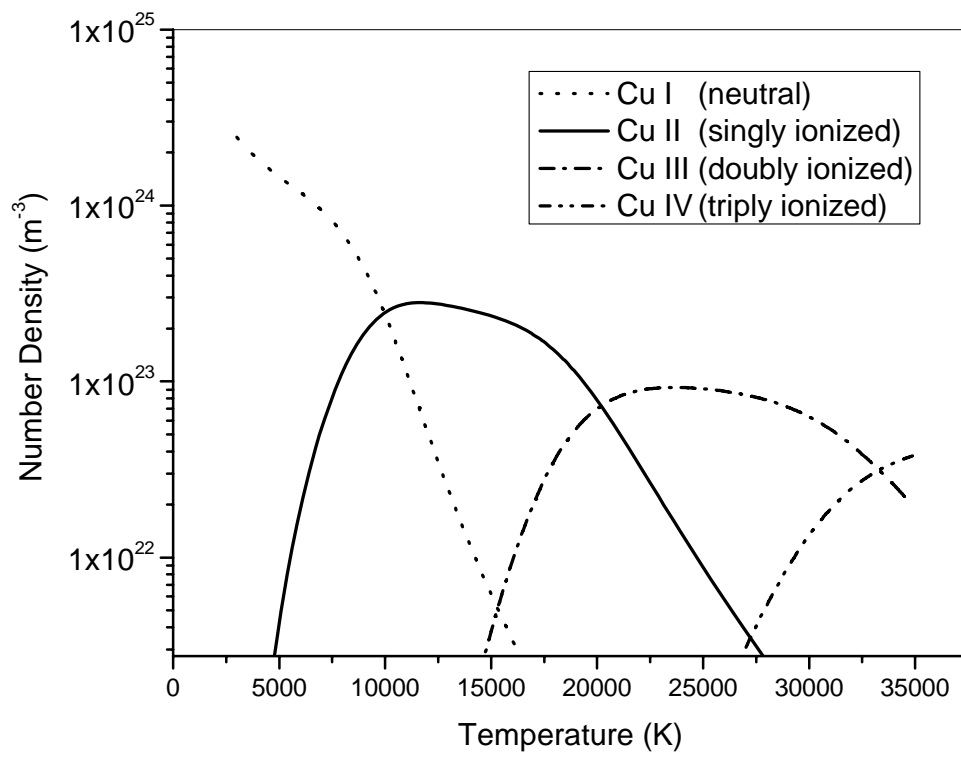


Figure 1. Equilibrium composition of a 1 atm pure copper vapor

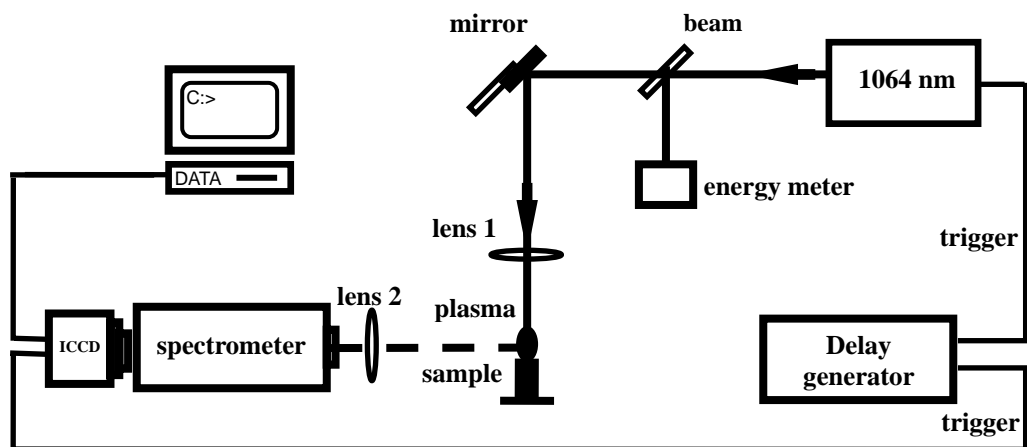


Figure 2. Experiment setup for ablating a target and time-resolved imaging of plasma properties.

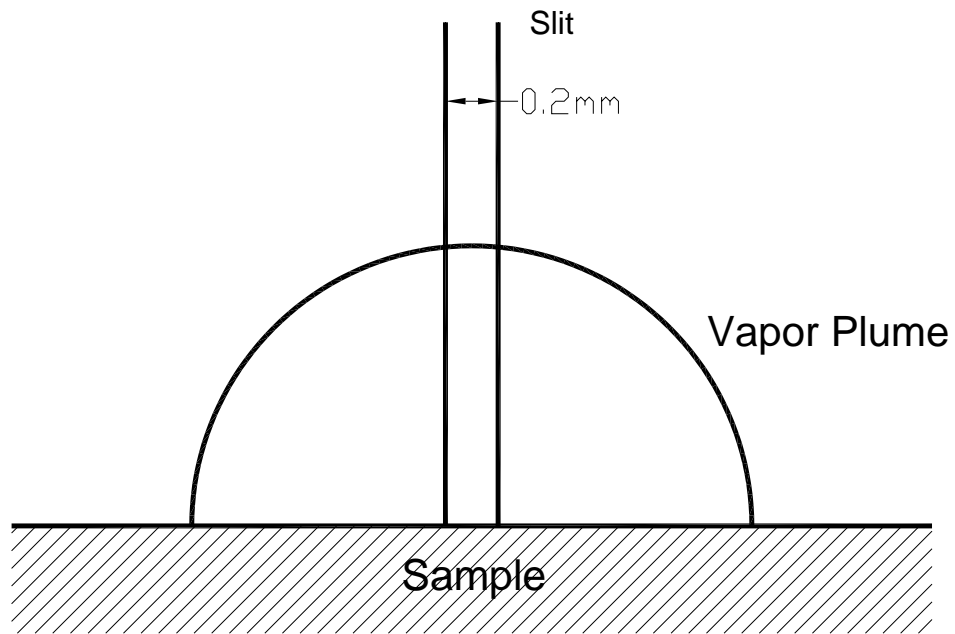


Figure 3. The spectrometer configuration used to image the plume. A 0.2mm slit was used along the longitudinal direction from the sample surface in order to capture the spatial temperature variation of the vapor plume.

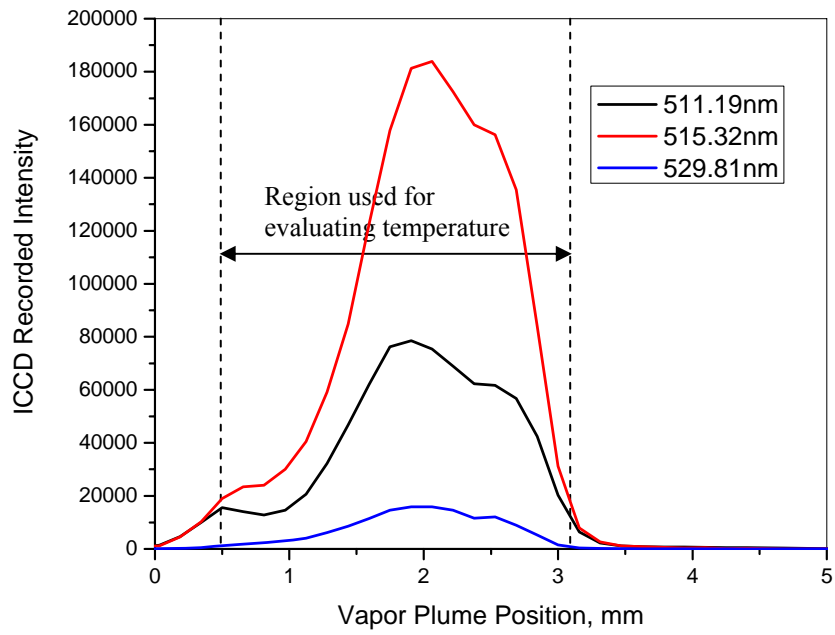


Figure 4. Spatial distribution of the emission intensity within the vapor plume for different spectral lines($E=100\text{mJ}$, image time= $10\text{ }\mu\text{s}$). Zero corresponds to the position of the sample surface.

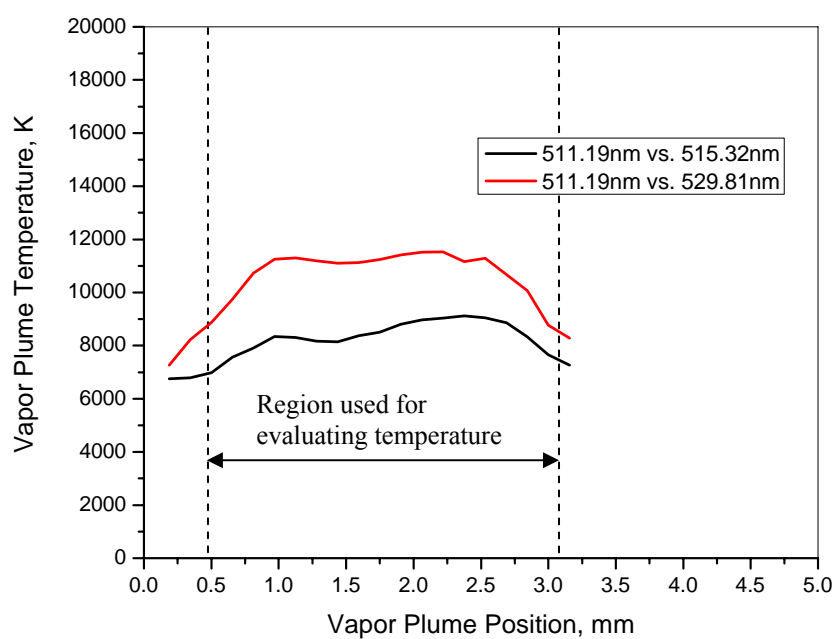


Figure 5. Spatial distribution of the temperature within the vapor plume calculated from different spectral lines($E=100\text{mJ}$, image time= $10\text{ }\mu\text{s}$). Zero corresponds to the position of the sample surface.

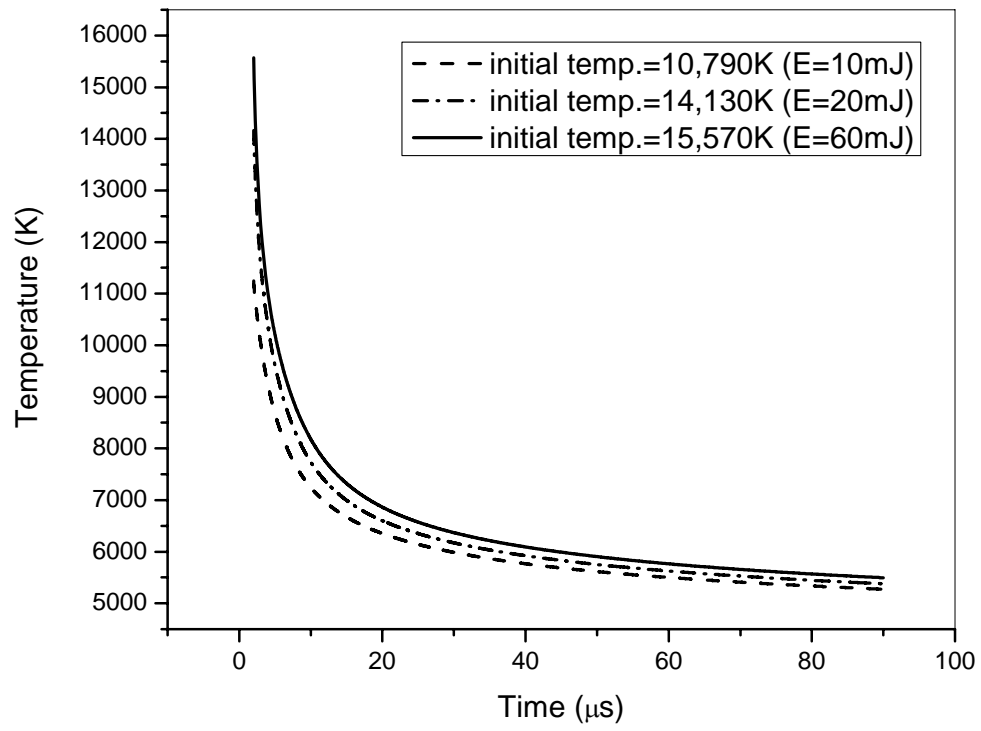


Figure 6. Simulation result for the temperature variation of the vapor plume for different laser energies.

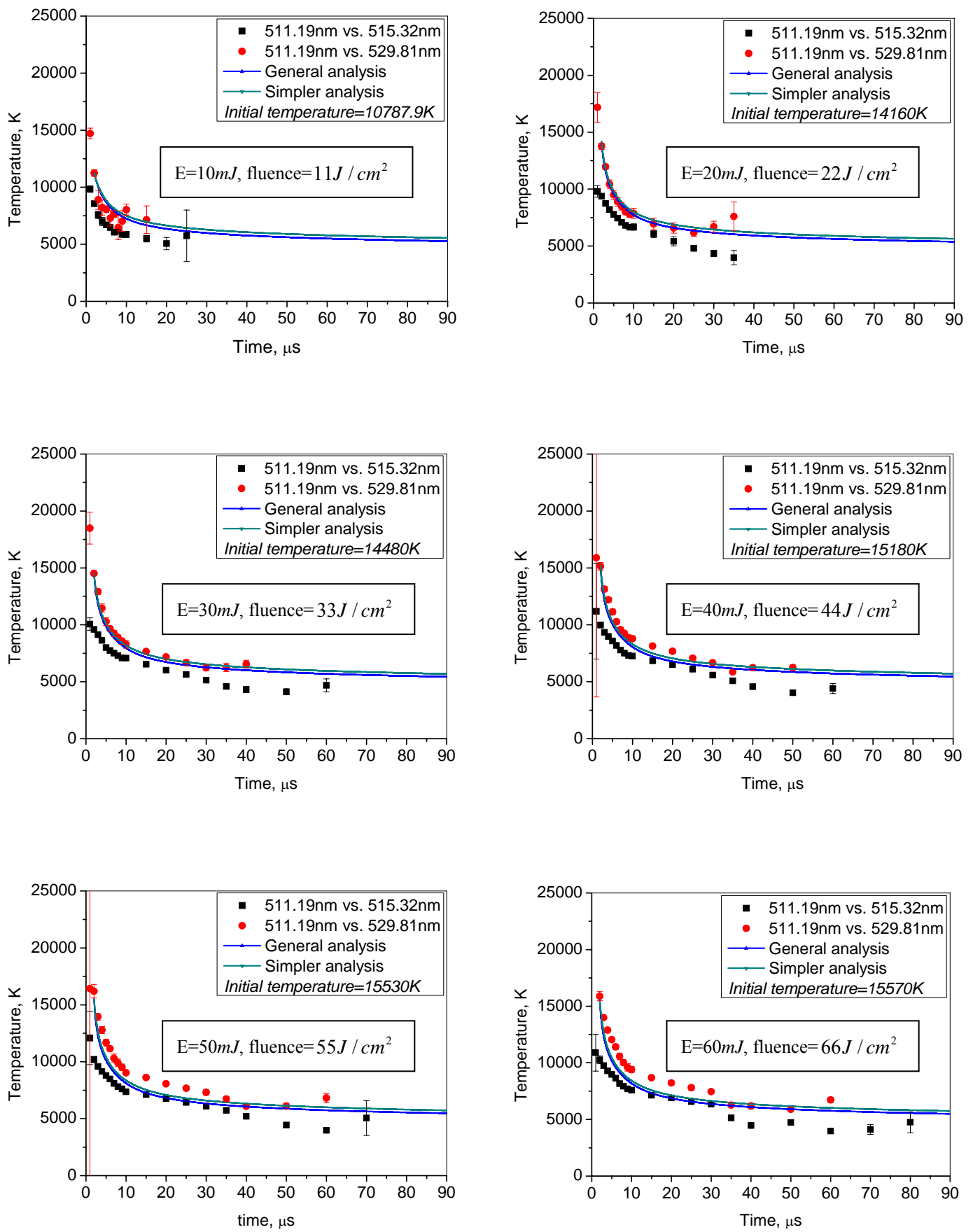
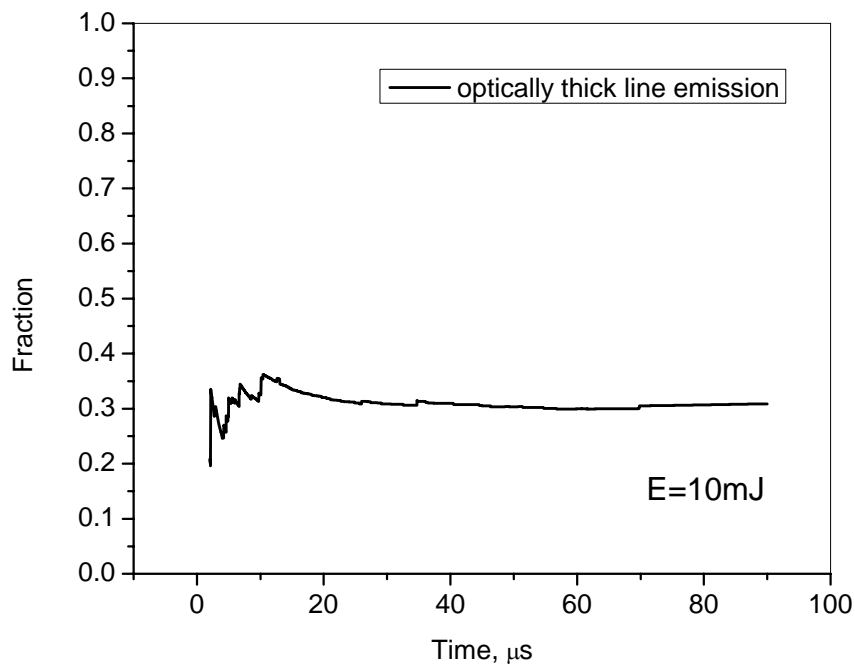
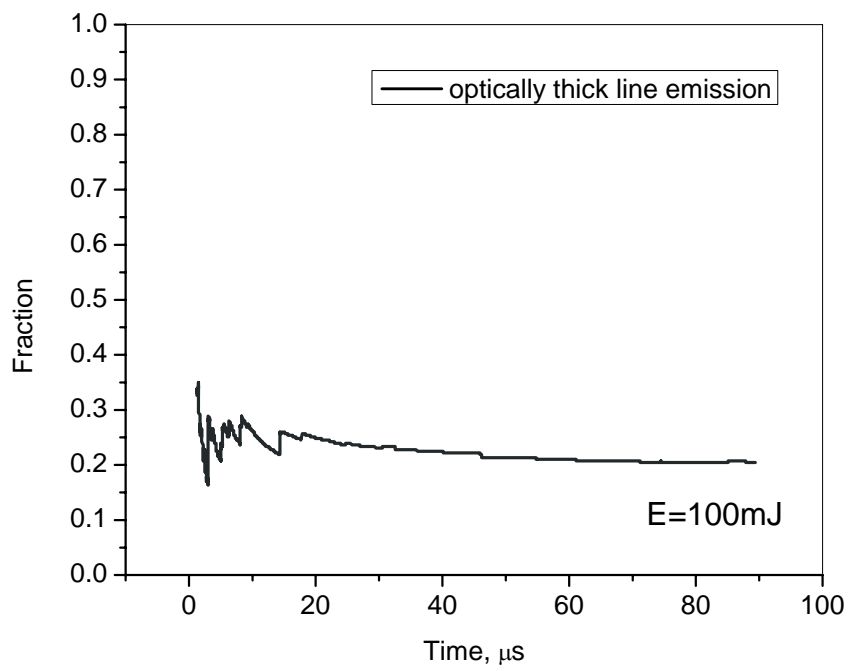


Figure 7. Comparison of the simulation results with the measurements of the temperature

of the vapor plume for different laser energies, $E(\text{mJ})$. (a) 10mJ (fluence= $11J / \text{cm}^2$) (b) 20mJ (fluence= $22J / \text{cm}^2$) (c) 30mJ (fluence= $33J / \text{cm}^2$) (d) 40mJ (fluence= $44J / \text{cm}^2$) (e) 50mJ (fluence= $55J / \text{cm}^2$) (f) 60mJ (fluence= $66J / \text{cm}^2$).



(a)



(b)

Figure 8. (a) Fraction of the optically thick lines contributing to the radiative heat transfer when $E=10\text{mJ}$ (b) Fraction of the optically thick lines contributing to the radiative heat transfer when $E=100\text{mJ}$

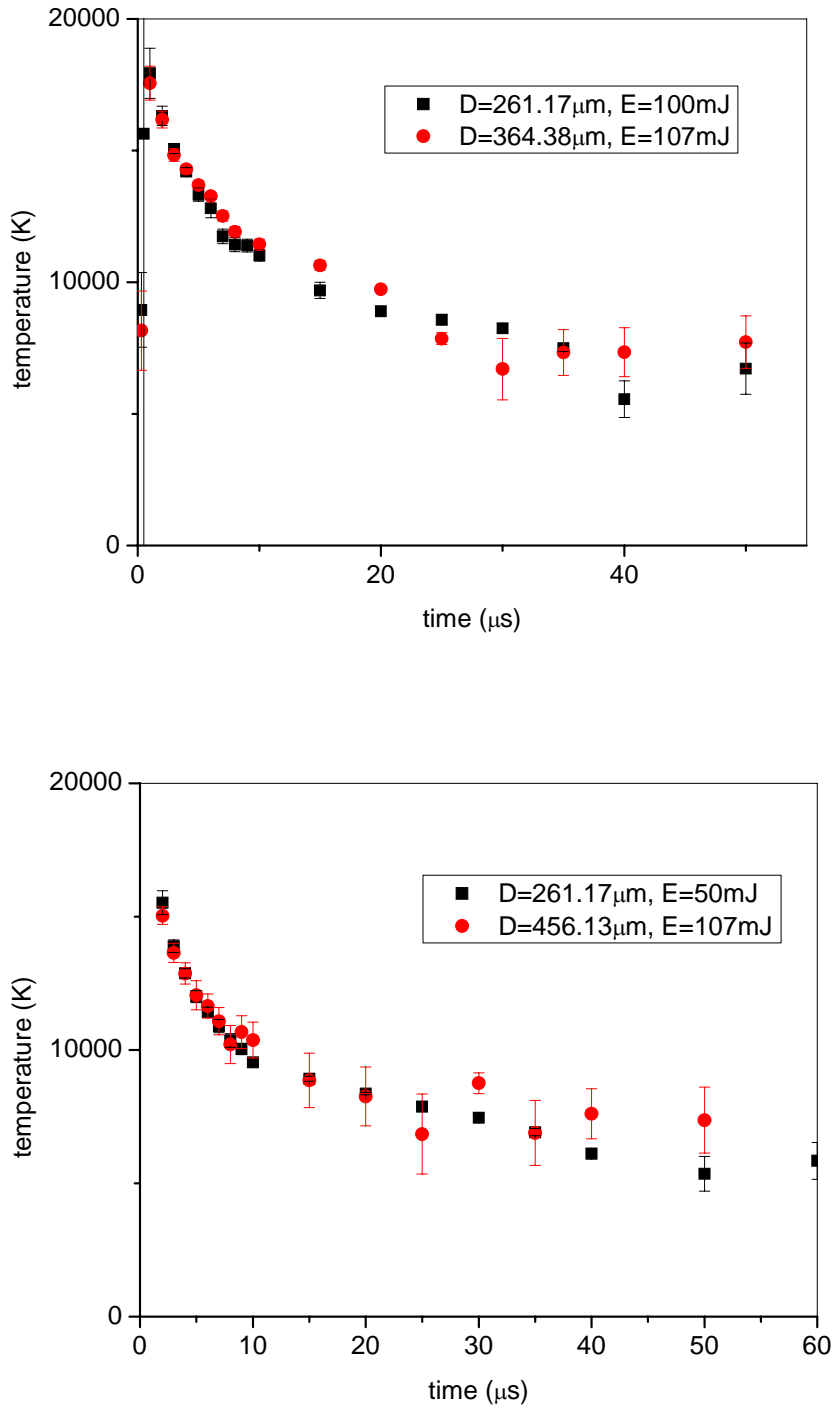


Figure 9. Temperature variations of vapor plumes with different spot size and laser energy but with similar initial plume temperature.

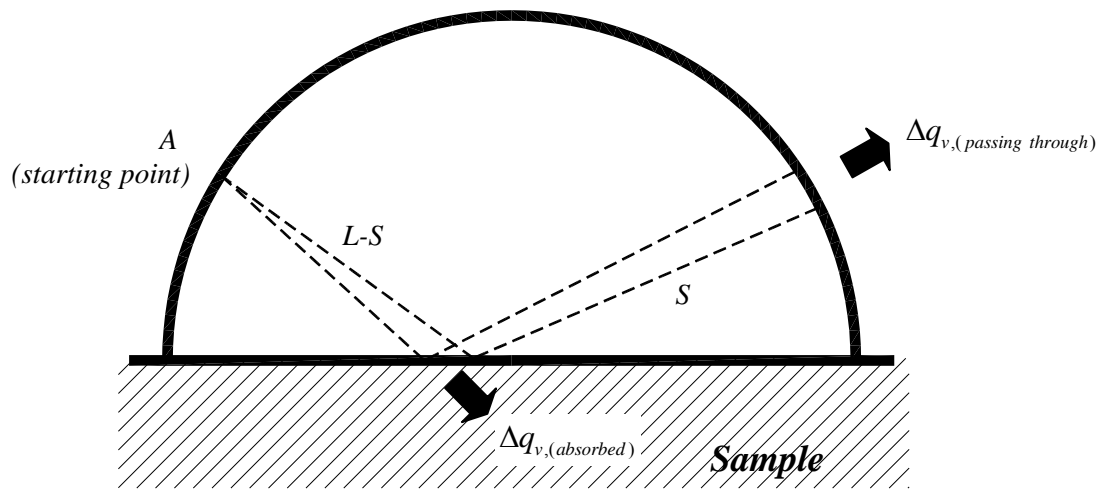


Figure 10. Schematic diagram of the radiative heat loss from the vapor plume starting at A which reaches the sample surface and specularly reflects through the vapor plume.

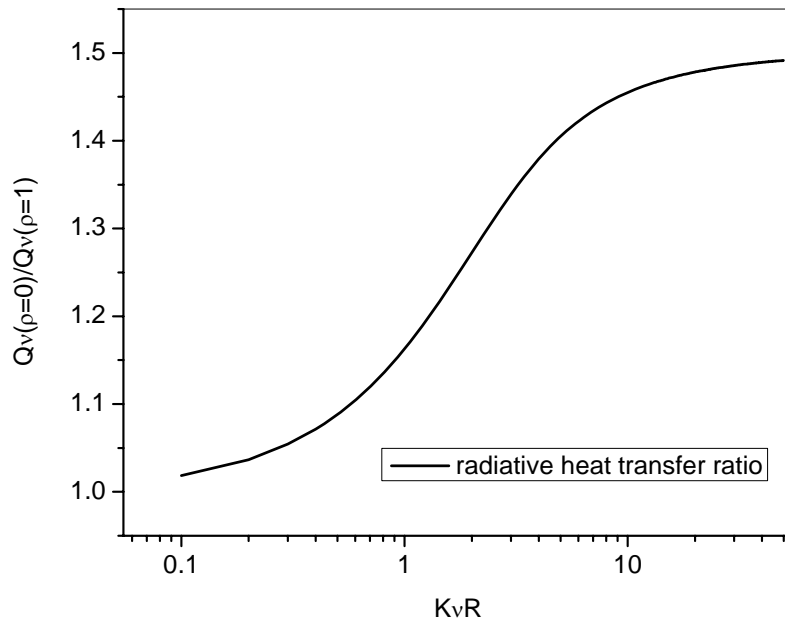


Figure 11. The spectral radiative heat transfer ratio between an ideal absorption surface, $\rho = 0$, and an ideal reflection sample surface, $\rho = 1$

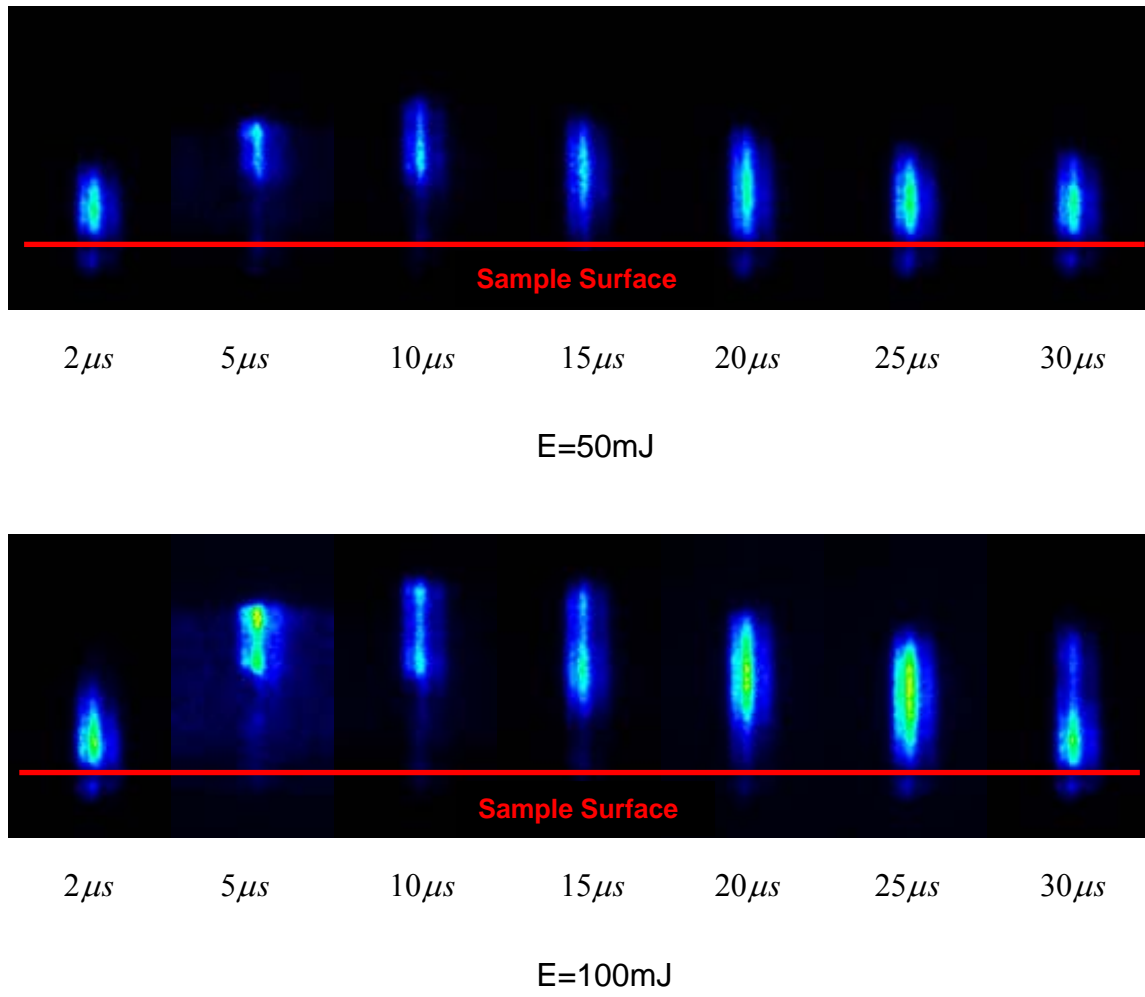


Figure 12. Spectral image of the 515.32nm emission line at different times after the laser pulse with $E=50\text{mJ}$, and $E=100\text{mJ}$ with spot size $\sim 170\mu\text{m}$.

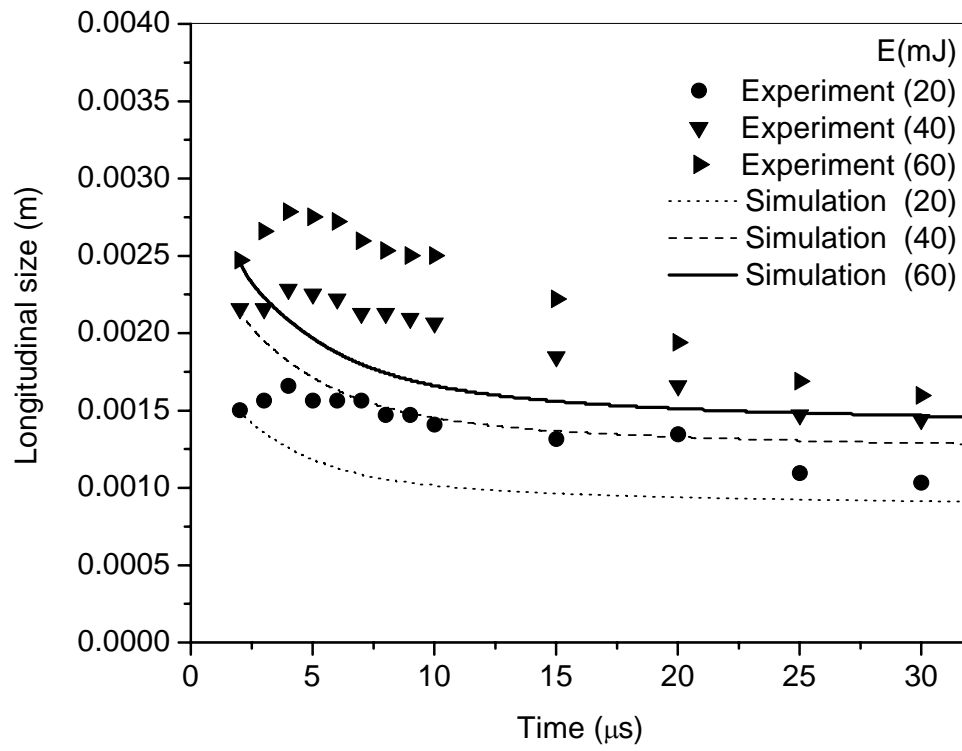


Figure 13. Comparison between simulated (by general line-by-line analysis) and experimental results of the vapor plume size under different laser energies.